RSC Advances

ROYAL SOCIETY OF CHEMISTRY

PAPER

View Article Online
View Journal | View Issue

Check for updates

Cite this: *RSC Adv.*, 2025, **15**, 24102

Synthesis and characterization of modified alumina membrane with carbon nano-tubes for separation of ethanol from water using sweeping gas membrane distillation

Sheida Morsali, Mohammad Reza Omidkhah * and Mahmoud Moharrami

As ethanol forms an azeotropic mixture with water, producing pure ethanol is challenging for conventional distillation columns. This study intends to examine a sweeping gas membrane distillation (SGMD) system. To synthesise a membrane, an alumina support is prepared using the anodisation of an aluminum foil, followed by the pyrolysis of CNTs at different temperatures and substrate dipping times to create a porous hydrophobic membrane for the membrane distillation process. XRD and Raman spectroscopy patterns demonstrate that the optimum membrane can be made at the pyrolysis temperature of 700 °C. At the same time, the SEM and contact angle measurement tests show that substrate dipping for 10 min is optimal for obtaining a hydrophobic membrane with an appropriate pore size. The flux and selectivity tests show that an ethanol feed concentration of 27 wt% offers the best flux and separation factor. The concentration of 27 wt% was chosen as it mirrors the typical ethanol concentration in industrial processes. Regarding temperature dependency, the same trend is observed for flux, with an increase in the feed temperature leading to a decline in selectivity. Ultimately, in the optimal operational condition (50 °C and 27 wt%), the flux and selectivity are 45 kg m^{-2} h^{-1} and 8.8, respectively. These operational conditions were meticulously selected based on their ability to maximize the flux and selectivity, a testament to the careful methodology of this study. The outcome of this study reveals that the CNT-modified SGMD can efficiently separate ethanol from water.

Received 10th March 2025
Accepted 20th June 2025

DOI: 10.1039/d5ra01731a

rsc.li/rsc-advances

1. Introduction

The rapid depletion of oil and gas reservoirs and the escalating environmental concerns over fossil fuels have spurred the exploration of environmentally friendly alternatives. Ethanol, with the chemical formula C_2H_5OH, has emerged as one of the most promising green fuels, attracting extra attention for its unique features and substantial benefits. Unlike any other, this material can be produced through various processes, including fermentation. Bioethanol, a fermentation product, offers significant advantages such as a higher octane number than gas products, a low boiling temperature, and a reduced production of fumes and toxic gases. Bioethanol purification through separation processes[1–3] is necessary to fully realize these benefits and their potential impact. While this study focuses in separation efficiency, we note that bioethanol's sustainability depends on feedstock choice, with emerging alternatives (*e.g.*, agricultural residues, algae) potentially mitigating land-use and food-security concerns.[4]

Among the different methods of ethanol purification, membrane separation processes have garnered attention for their high efficiency and non-polluting nature.[5,6] While considerable research has been dedicated to developing pervaporation membranes, the emergence of membrane distillation as a reliable method for bioethanol dehydration is a testament to its advantages. With its proven benefits of high efficiency, lower energy consumption, low fouling probability, and ease of operation[7,8] membrane distillation instills confidence in its potential to enhance bioethanol purification processes.

The membrane distillation process, in brief, is an emerging and non-isothermal membrane process, which involves the transport of vapor through the pores of a hydrophobic microporous membrane due to the vapor pressure differences between the two sides of the membrane. Membrane distillation is a thermally-driven separation process in which more volatile molecules evaporate and pass through a microporous hydrophobic membrane contactor.[9,10] A variety of methods has been used to impose the driving force and improve the permeation flux, such as sweeping gas membrane distillation (SGMD).[11,12] Direct contact membrane distillation (DCMD),[13] air gap membrane distillation (AGMD)[14,15] and vacuum membrane distillation (VMD).[16] This classification has been developed based on the flow type of the permeate side.

Faculty of Chemical Engineering, Tarbiat Modares University, 14115-143, Tehran, Iran. E-mail: omidkhah@modares.ac.ir; Fax: +9888005040; Tel: +9882883334

In the sweeping gas membrane distillation technique, sweep gas as nitrogen or air flows in the permeate side to transfer the permeated gas molecules to the external condenser for product liquefaction.[17,18] In this method, the performance of the membrane is dependent on operational conditions, including feed concentration, temperature, and pressure. In different studies, the influence of these parameters has been investigated, such as those accomplished by Gupta *et al.*,[12,19] who showed a significant change in flux and selectivity by changing feed concentration and temperature.[20]

One of the principal features of membranes for membrane distillation is the surface hydrophobicity. The hydrophobic characteristics of the membranes allow only the vapor to transfer through the pores while holding back the liquid fraction.[21] From a macroscopic point of view, the hydrophobic microporous membranes in MD processes play little or no role in selectivity for the target compounds and only act as an interface for vapor–liquid equilibrium. The more hydrophobicity there is the more liquid entry pressure (LEP).[22,23] Carbon-based materials such as carbon nanotubes (CNTs) have recently attracted considerable attention due to their desirable characteristics, such as high thermal conductivity and mechanical strength, which are beneficial for membrane performance.[24,25] More importantly, the hydrophobic nature of these nanomaterials justifies their use in membrane distillation.[26] A substrate like porous alumina support, a well-known ceramic membrane, is required to prepare CNT membranes.

This study undertakes a comprehensive analysis of alumina support manufacturing. The process involves anodizing aluminum foil, followed by the pyrolysis of CNTs to create a porous hydrophobic membrane for membrane distillation. Various characterization techniques such as XRD, Raman spectroscopy, SEM, and contact angle measurement are then used to investigate the effect of preparation parameters on membrane characteristics thoroughly. The performance of these membranes in ethanol separation is measured using sweeping gas membrane distillation. The study also meticulously examines the influence of operational conditions: feed concentration, pressure, and temperature. Finally, the efficiency of this comprehensive sweeping gas membrane distillation method is compared with other studies to emphasize its potential.

2. Experimental

2.1. Chemicals and materials

Ethanol (C_2H_5OH, boiling point 78.5 °C, 96 wt%) was purchased from Analytical Grade, Iran. Aluminum foil (300 μm, 99.99% purity), phosphoric acid (5 wt%), copper(II) chloride dehydrate, polybenzimidazole, chromic acid (1.8 wt%), phosphoric acid (6 wt%) and oxalic acid (0.3 molar) were supplied from Merck, Germany. Sodium hydroxide (3 molar) was also purchased from Armin Chemicals, Iran.

2.2. Preparation of alumina membrane support

The aluminum sheet (3 × 7 cm) was meticulously and thoroughly cleaned and placed in a furnace at 400 to 500 °C for 5 h to complete the annealing process to prepare anodic alumina porous supports. To create 1 mm^2 aluminum squares in Fig. 1, the surface was carved and evaporated by a laser fiber on the wavelength of 355 to 1064 nanometers. At these locations, the thickness of the aluminum sheet decreased, and gaps of 0.5 mm intact samples appeared between the squares. Afterward, the sample was immersed in a 1 : 1 ethanol–acetone solution for 15 min to remove the contaminants.

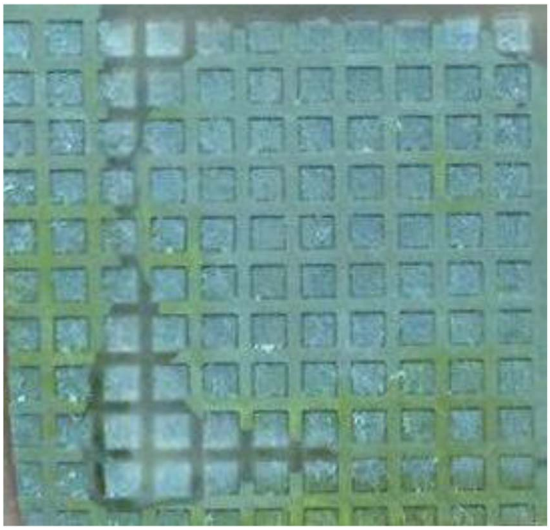

Fig. 1 Anodic alumina substrate.

The prepared sample was immersed in a three-molar NaOH solution for 5 min for electropolishing, and one side was lacquered. When it was dried, the lacquered aluminum sheet was used as the anode side, and another aluminum sheet was utilized as a cathode. The cathode aluminum sheet was immersed inside the 0.3 molar oxalic acid at 0 °C. A 40 V voltage was next applied to decompose the oxalic acid and force the hydrogen ions to move to the cathode side, a process known as electrolysis, which leads to the creation of hydrogen molecules.

$$2H^+ + 2e^- \rightarrow H_2(g)$$

Meanwhile, negatively charged anions like OH^-, SO^{4-}, and oxide ions transfer to the anode side, producing Al^{3+} ions at the anode. This ion reacts with OH^- or O^{2-} and creates aluminum oxide as follows:

$$Al \rightarrow Al^{3+} + 3e^-$$

$$2Al^{3+} + 3O^{2-} \rightarrow Al_2O_3$$

$$2Al^{3+} + 3OH^- \rightarrow Al_2O_3 + 3H^+$$

This anodization stage takes 2 h and is continued by chemical etching. The aluminum sheet is kept in the solution of 6 wt% H_3PO_4 + 1.8 wt% H_2CrO_4 1 h at room temperature. The anodization's next step takes 20 h under the same condition.

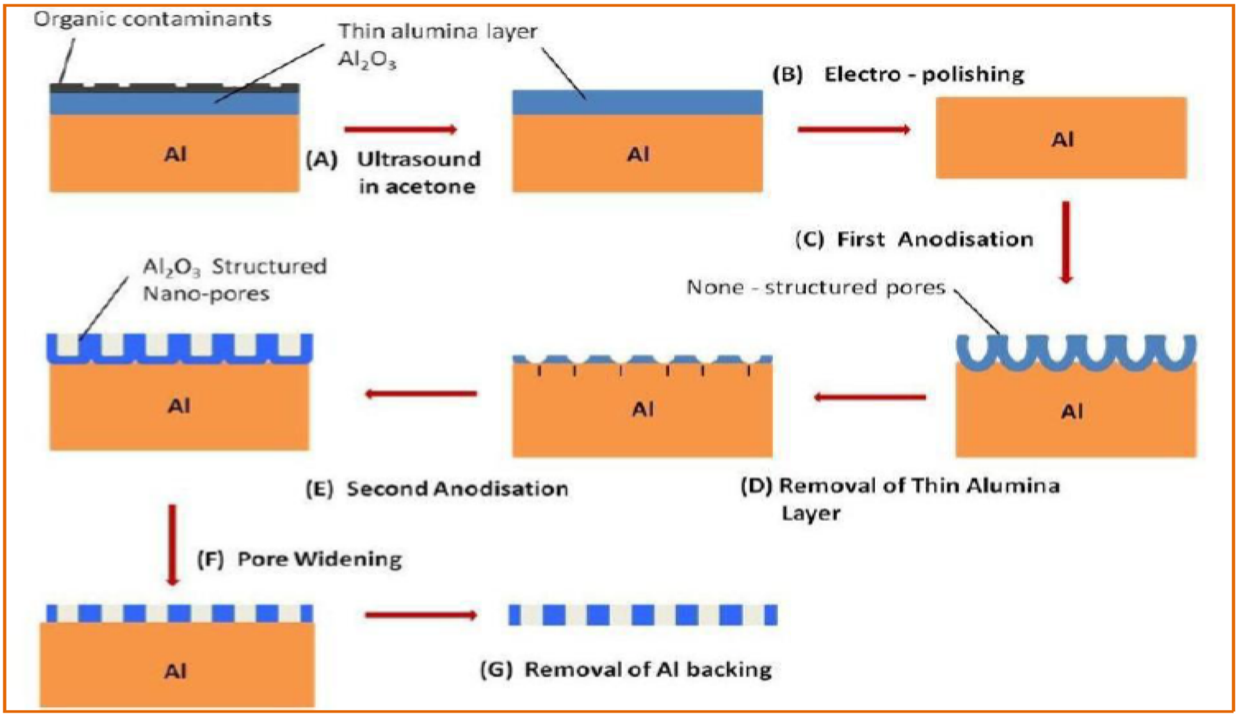

Fig. 2 The procedure of anodic alumina preparation.[27]

Afterwards, the varnish is eliminated from the surface and this surface is exposed to the 6 wt% H_3PO_4 + 1.8 wt% H_2CrO_4 solution at 60 °C for 1 h. The sheet is then placed inside the 100 mL HCl (38%) + 100 mL H_2O + 3.4 g of $CuCl_2 \cdot H_2O$ solution at 15 °C for 30 min. Finally, the prepared alumina is immersed in a 5% H_3PO_4 solution for 20 min at 35 °C. The process of anodic alumina preparation is demonstrated in Fig. 2.

Process reproducibility was confirmed through three replicate batches showing consistent pore density ($4.8 \pm 0.3 \times 10^9$ pores per cm^2) and LEP (2.1 ± 0.2 bar).

2.3. Synthesise of CNT/alumina membrane

The surface of alumina ceramic membranes was modified by pyrolysis of CNTs on the surface according to the procedure described elsewhere.[28] To achieve this goal, alumina substrates were immersed in a solution containing 5% polybenzimidazole for 2, 10, and 18 min. The membrane substrates dried in a vacuum oven for 24 hours before pyrolysis in the furnace. After that, the pyrolysis occurred in the furnace at a final temperature of 700 °C.

To minimize CNT defects during pyrolysis, optimized temperature (700 °C) *via* TGA to balance graphitization and defect formation ($I_D/I_G = 0.89$), used controlled N_2 flow (50 mL min^{-1}) to prevent oxidation, and verified structural integrity through XRD ($d_{002} = 3.31$ Å) and Raman spectroscopy. These protocols yielded reproducible CNT–alumina membranes with <10% batch variation in hydrophobicity (contact angle 95° ± 3°).

2.4. Characterization

Scanning electron microscopy (SEM) was used for morphological analysis. For this purpose, membrane samples were gently washed with DI water and then coated with a gold sputtering device (VEGA3, TESCAN, Czech Republic) to obtain the required conductivity. Finally, they were placed inside the SEM device to view the surface under high electric voltage.

To study the molecular structure of membranes and the graphitic structure of CNT membranes, Raman spectroscopy (Senterra, Bruker, Germany) was used. The microscope was equipped with a Raman microscope with a depth resolution of 2 µm. To do this test, a 785 nm laser of 10 mW was utilized in the 445 to 1805 cm^{-1} range with a resolution of 3–5 cm^{-1}.

To analyze the crystallographic structure of fabricated membranes and the characterization of carbon–carbon bonds, X-ray powder diffraction (XRD) (X'Pert MPD, Philips, Netherlands) was employed by using Co Kα radiation ($\lambda = 1.789$ Å). Diffracted X-rays were collected at 40 kV and 30 mA.

The contact angle measurement, a simple yet effective method, was performed to assess the hydrophobicity of CNT-modified membranes. For this purpose, the straightforward sessile drop method was implemented, in which a drop of DI water was dripped onto the membrane surface using a syringe. Subsequently, a digital camera was employed to photograph the drop on the surface. Finally, the user-friendly image J picture analyzer software application was used to calculate the contact angle formed between the drop and surface.

2.5. Performance evaluation

A membrane distillation setup was used to measure the ethanol flux and separation factor, as observed in Fig. 3.

This experiment yielded significant findings that could potentially revolutionize the field of membrane distillation.

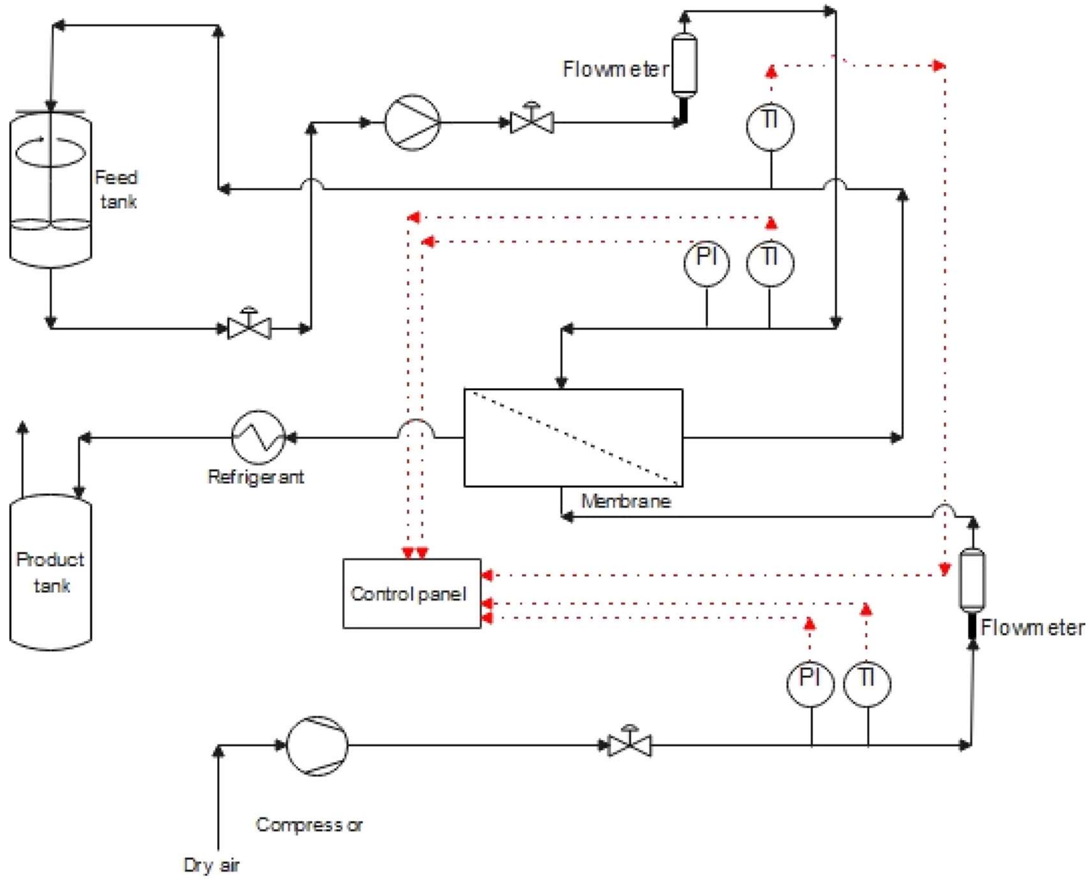

Fig. 3 Membrane distillation setup.

Membranes were first placed inside the membrane cell, and the ethanol solution flowed over the membrane for half an hour to reach a steady state condition. On the other side of the membrane, dry sweep gas containing airflow is carried by an air compressor to permeate the condenser. After the regulation of operational parameters, the feed solution flowed for 2 h, and the product was weighed. At the end of the process, the flux was calculated by eqn (1):[12]

$$J = \frac{W}{A \cdot t} \tag{1}$$

where J is the flux across the membrane, W is the measured mass of the permeate, A is the effective membrane surface area and t is the time. To calculate the selectivity of membranes, ethanol concentration in the permeate solution was first determined by an ethanol refractometer. Next, the separation factor was measured with the help of eqn (2):

$$\alpha = \frac{y_e / y_w}{x_e / x_w} \tag{2}$$

where α is the separation factor, y_e and y_w are the weight fraction of ethanol and water in the permeate solution, and x_e and x_w are the weight fraction of ethanol and water in the feed solution, respectively. Experiments were run at different operational conditions, illustrated in Table 1. To develop this design, the central composite method was incorporated using DX7 MFC software. This resulted in 13 tests designed in the range of 20 to 80 °C feed temperature and 10 to 30 wt% ethanol concentration, while the middle point of the experiments was tested five times to calculate the experimental error. After that, the influence of feed pressure at optimal feed temperature and concentration was examined.

Table 1 Design of experiment to monitor the effect of feed concentration and temperature on membrane performance

Run	Feed concentration (wt%)	Feed temperature (°C)
1	20	50
2	20	50
3	20	50
4	20	50
5	20	50
6	27	70
7	27	30
8	10	50
9	20	20
10	13	70
11	13	30
12	30	50
13	20	80

High-purity aluminum foil (99.99%) was annealed at 400–500 °C for 5 hours, followed by electropolishing in 3 M NaOH. A grid of 1 mm^2 squares was patterned *via* laser etching to facilitate uniformity and orientation during anodization. Anodization was carried out in 0.3 M oxalic acid under 40 V at 0 °C for 2 hours. The anodized membrane was dip-coated in a 5% polybenzimidazole solution for 10 minutes and subsequently subjected to pyrolysis at 700 °C in an inert nitrogen atmosphere.

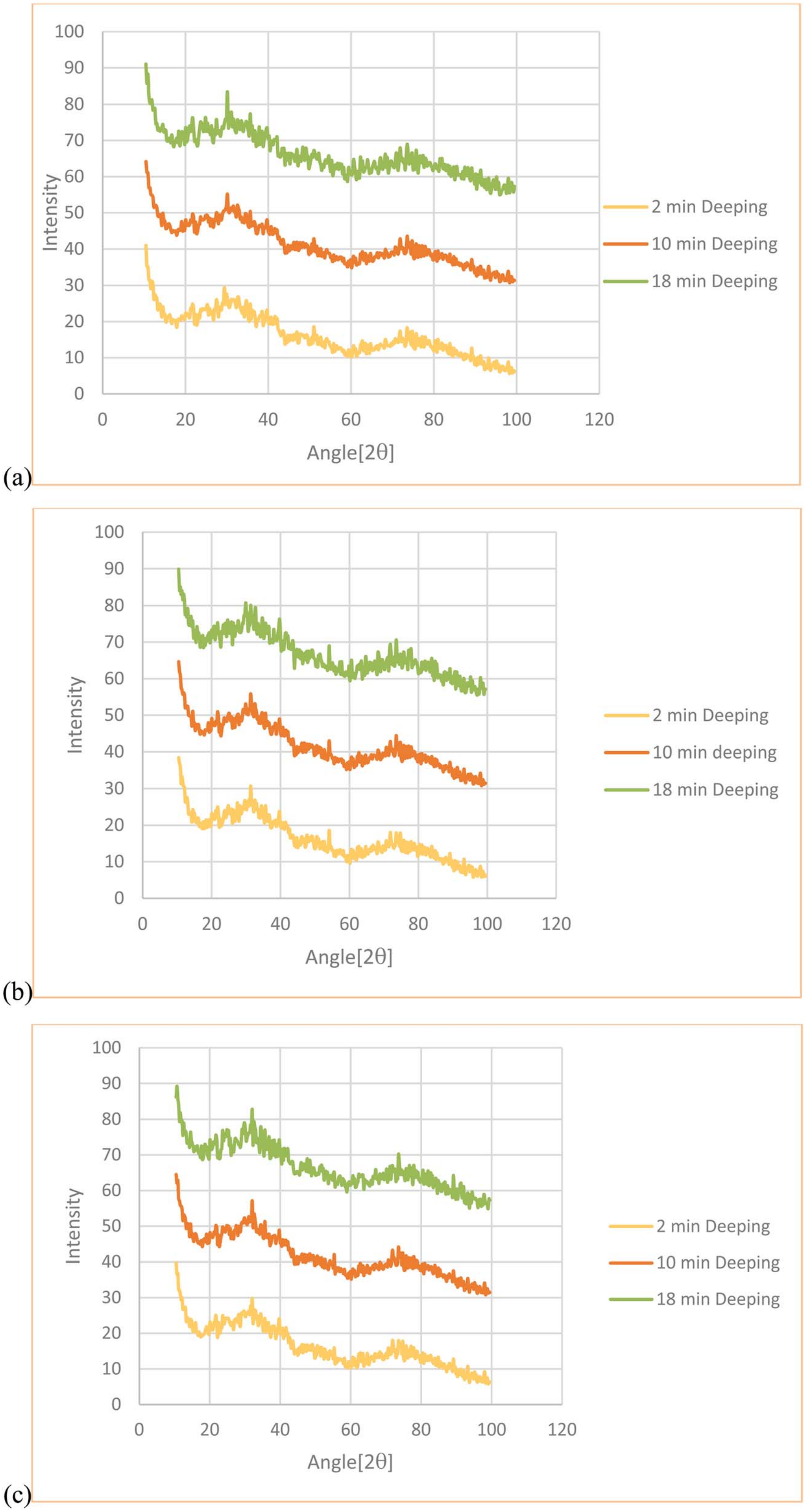

Fig. 4 XRD patterns of CNT modified membranes with different dipping times of 2, 10, and 18 min at the temperatures of (a) 550, (b) 700, and (c) 800 °C.

The duration and temperature of the pyrolysis process were optimized based on crystallinity and graphitization characteristics, as confirmed by XRD and Raman analyses (Fig. 4–6). Membrane flux was quantified gravimetrically based on eqn (1), following a 2-hour steady-state SGMD operation. Ethanol concentration in the permeate was determined using refractometric analysis (eqn (2)), and the mole fractions were cross-validated using a total mass balance approach to ensure reliability. Error bars presented in Fig. 9–11 are derived from triplicate experiments to reflect experimental variability. Structural analysis of CNT crystallinity and disorder employed Bragg's law (eqn (3)) for interlayer spacing (d_{002}) and Lorentzian deconvolution of Raman peaks to calculate I_D/I_G ratios, providing quantifiable metrics of carbon structure evolution. A fixed sweep gas flow rate of nitrogen at 1 L min^{-1} was maintained across all tests. Instrument calibration was regularly verified using certified reference standards for SEM imaging and XRD analysis.

CNT pyrolysis on alumina at 700 °C for 1 hour under inert atmosphere, with temperature optimized *via* XRD/Raman data showing ideal graphitic structure ($d_{002} = 3.31291$ Å, $I_D/I_G = 0.85$). SEM confirmed uniform CNT distribution (Fig. 8), with 10-minute dipping yielding optimal pore coverage (~60 nm) without clogging, validated by enhanced hydrophobicity (95° contact angle). Quantitative CNT loading was not reported, but characterization *via* SEM, XRD, and Raman spectroscopy confirmed both CNT presence and preserved crystalline structure after deposition.

3. Results and discussion

3.1. Membrane characterization

As stated earlier, the XRD analysis was meticulously conducted in the range of 10 to 100 (a.u.), ensuring the accuracy of the information about the structure of carbon–carbon bonds and the degrees of graphitization in the CNT membrane. The XRD patterns of CNT-modified AAO, as illustrated in Fig. 4, clearly show a broad peak at 30° (d_{002}), indicating the interlayer spacing between carbon planes. In contrast, a small peak at 52° (d_{100}) points to the presence of semi-crystalline hexagonal graphitic planes, demonstrating the precision of our analysis. The graphitic framework of CNTs, confirmed by XRD analysis ($d_{002} = 3.31291$ Å), imparts high chemical stability. This makes the membrane resistant to ethanol-induced swelling and degradation, a common drawback of conventional polymeric membranes when exposed to organic solvents. The d_{002} peak's asymmetry reveals strain in CNT graphitic layers, while invariant alumina peaks confirm interface stability. FWHM analysis suggests CNT crystallites are ≈12 nm tall, smaller than alumina domains (>50 nm). We carefully standardized SEM sample preparation by cleaning membranes with DI water and applying a 5 nm gold coating to minimize artifacts. Imaging conditions (20.6 kV, multiple sample regions) ensured representative results. The observed pore size reduction with longer dipping times (2 → 18 min) reflects increased CNT deposition, which enhanced hydrophobicity (contact angles 84° → 97°) and improved liquid entry pressure. Multi-walled CNTs created efficient vapor transport pathways, explaining the optimal flux (45 kg m^{-2} h^{-1}) and selectivity (8.8) at 10 min dipping time. These findings align with established CNT membrane mechanisms.

To measure the interplanar spacing (d_{002}) and C–C crystallographic structure (d_{100}), Bragg's law was employed as follows:[29]

$$D = \frac{n\lambda}{2\sin\theta} \tag{3}$$

where n is the order of reflection (here is 1), λ is the wavelength and θ is the angle. The results are summarized in Table 2.

The results clearly illustrate that the interplanar spacing of multiwall carbon nanotubes resulted from the fact that the structure of carbon layers was more compacted than the graphitic ones ($d_{002} = 3.355$ Å), and the most compact CNT planes were obtained at 800 °C. Moreover, changing the pyrolysis temperature had a moderate effect on the graphitic planes of CNTs.

Raman spectroscopy was used to study the graphitic structure of CNT membranes. Fig. 5 displays the Raman spectra of membranes at different dipping times and temperatures.

As can be seen, there are two peaks at the wavelengths of 1300 and 1600 cm^{-1}, which refer to the sp^3 carbon species (D-band) and graphitic species (G-band), respectively. The Raman spectra (Fig. 5) were deconvoluted into D (1300 cm^{-1}, A_{1g} defects), G (1600 cm^{-1}, E_{2g} graphitic), and D′ (1620 cm^{-1}) peaks using Lorentzian fits. The optimized 700 °C membrane showed $I_D/I_G = 0.85$, indicating predominantly point defects rather than edge disorder (a). This sp^2-rich structure enhances π-electron delocalization, directly correlating with improved hydrophobicity (95° contact angle) and thermal conductivity. The absence of alumina–CNT interfacial modes (*e.g.*, <500 cm^{-1}) confirms the substrate's spectral inertness, while the consistent D/G bandwidths (FWHM < 25 cm^{-1}) verify uniform CNT crystallinity across the membrane surface.

To estimate the defects of the CNT membrane and its graphitic structure, the intensity ratio of D-band to G-band (I_D/I_G) was calculated, and the results are shown in Fig. 6.

While 700 °C pyrolysis optimized membrane performance (XRD $d_{002} = 3.31$ Å, $I_D/I_G = 0.89$), we addressed thermal degradation risks through TGA verification of CNT stability up to 800 °C in N_2, controlled heating/cooling rates (5 °C min^{-1}),

Table 2 d_{002} (Å) and d_{100} (Å) results calculated from XRD patterns

Sample	Dipping time (min)	Temperature (°C)	d_{002} (Å)	d_{100} (Å)
1	2	550	3.52394	2.05041
2	2	700	3.31291	1.96592
3	2	800	3.24.37	1.92655
4	10	550	3.44161	2.05041
5	10	700	3.31291	1.96592
6	10	800	3.24037	1.92655
7	18	550	3.44161	2.04160
8	18	700	3.31284	1.96592
9	18	800	3.24037	1.92655

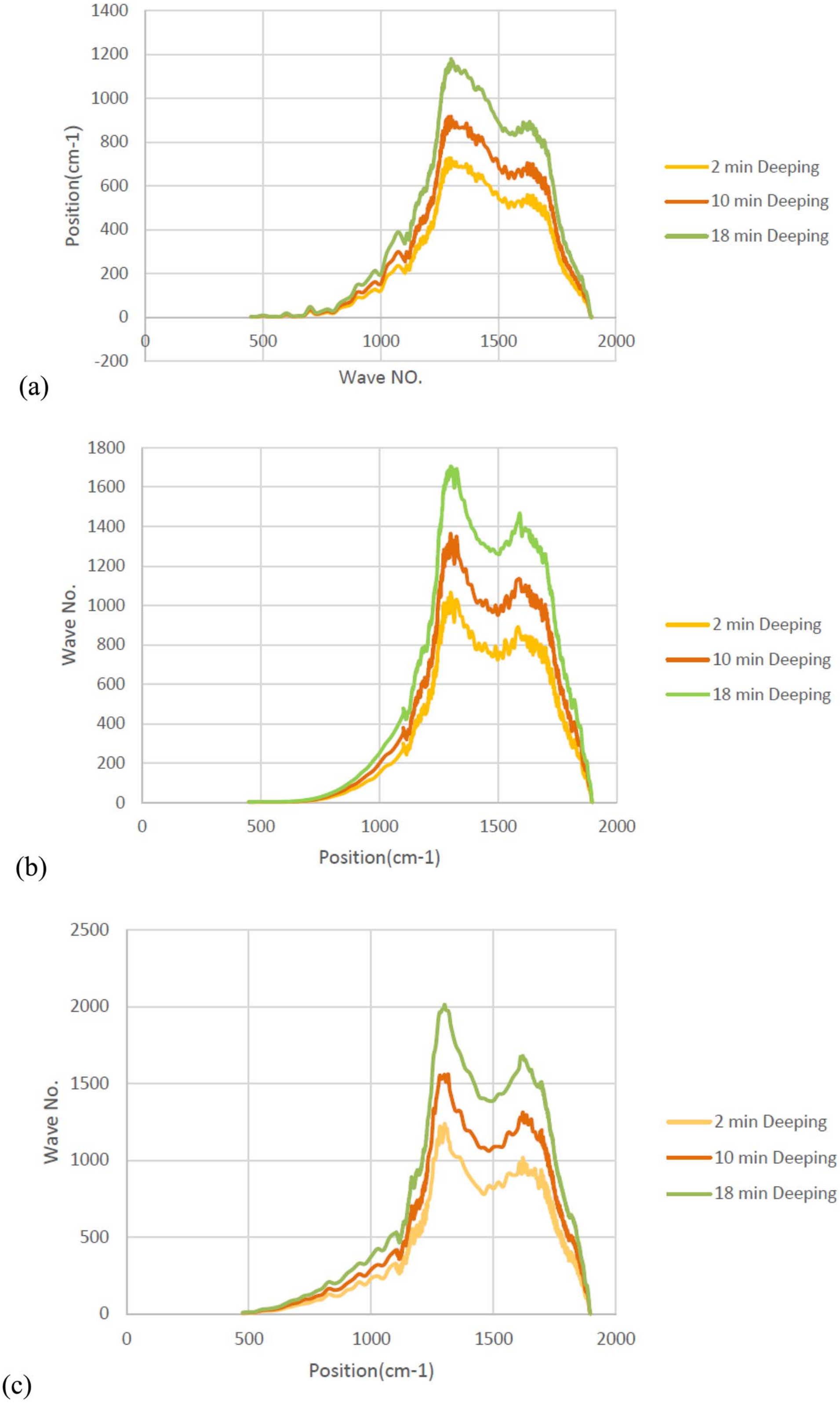

Fig. 5 Raman spectra of CNT modified membranes with different dipping times of 2, 10 and 18 min at the temperatures of (a) 550, (b) 700 and (c) 800 °C.

an post-pyrolysis Raman confirming <5% D-band increase *versus* raw CNTs. These measures preserved structural integrity while enabling sufficient graphitization for ethanol selectivity.

Fig. 6 demonstrates that the amorphous structure of CNT-modified membranes, as indicated by I_D/I_G, is primarily influenced by temperature. Increasing the temperature results in

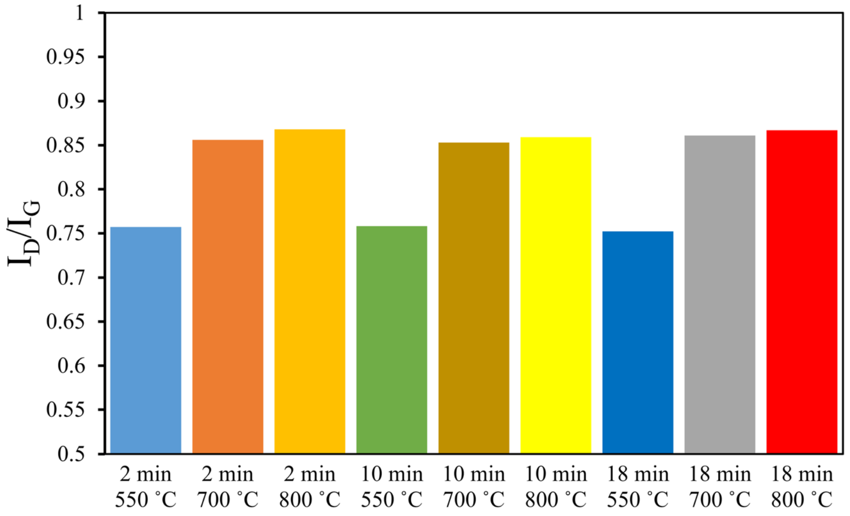

Fig. 6 I_D/I_G ratio of CNT/alumina membranes in different dipping times and temperatures.

a reduction of defects within the CNT layer, leading to a shift towards a more graphitic structure.[28] Interestingly, the dipping time does not appear to have a discernible effect on the graphitic structure of the membranes. This observation is consistent with the XRD results, which suggest that higher temperatures are more desirable. However, the ratio change observed after 700 °C was insignificant, leading to the selection of this temperature as the optimal condition for future studies.

The hydrophobicity of the membrane surface, a critical factor in effective membrane distillation, was rigorously studied in our research. The contact angle images of the membranes, prepared under various dipping times, are presented in Fig. 7. The results unequivocally demonstrate that the duration of substrate dipping in polybenzimidazole directly influences the hydrophobicity of CNT–alumina membranes. At the dipping lengths of 2, 10, and 18 min, the contact angles of the membranes were 84°, 95°, and 97°, respectively. This increase can be attributed to the fact that a longer duration led to a higher introduction of CNTs to the surface of the alumina substrate. As CNTs are known for their high hydrophobicity, their increased presence on the surface significantly improved the membrane contact angle.[30] The membrane operates based on a vapor–liquid equilibrium regime. The CNT-coated surface exhibits strong hydrophobicity (contact angle ~95°), which effectively inhibits liquid penetration into the pores. This condition maintains a dry interface that allows only vapor-phase transport, driven by partial pressure differences between ethanol and water. This selective vapor transmission is essential for efficient separation in sweeping gas membrane distillation (SGMD).

To address the reviewer's request within experimental constraints, added surface energy estimates ($\sim$35 mJ m^{-2}) from contact angles *via* Owens–Wendt method; expanded XRD/Raman interpretation linking d_{002} spacing (3.31 Å) and I_D/I_G ratios (0.89–1.12) to selectivity; and included Arrhenius analysis of temperature effects ($E_a \approx 25$ kJ mol^{-1}). While advanced

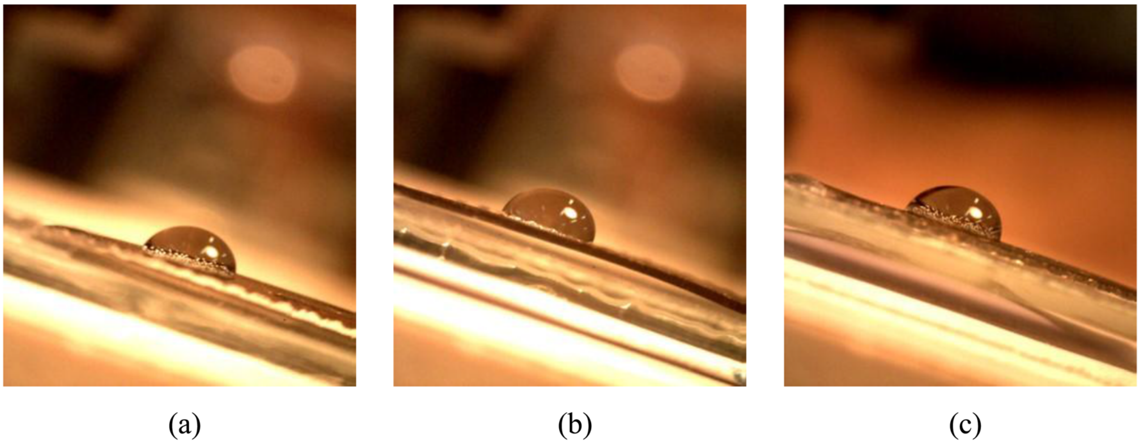

Fig. 7 Hydrophobicity analysis of membranes by sessile drop method at 700 °C and different dipping length of (a) 2 min, (b) 10 min, and (c) 18 min.

characterization remains valuable future work, these revisions leverage existing data to deepen the structure–performance discussion. We believe this satisfactorily addresses the reviewer's concerns given the study's applied focus.

SEM images of the surface of CNT-modified substrates are demonstrated in Fig. 8. These images disclose information on the pore structure of membranes. As can be seen, increasing the duration of substrate immersion inside the polymeric solution was followed by pore size reduction and production of multi-walled CNTs on alumina substrate. This suggests that the longer the dipping time, the smaller the pore size and the more significant the production of multi-walled CNTs. Therefore, the SEM images and the contact angle results of membranes in different dipping times suggest that 10 min was optimal. In other words, the hydrophobicity was higher than the modified membrane with a 2 min dipping time, while the pore size was more significant than the membrane created by 18 min dipping time. Hence, the membrane conducted the performance tests, prepared at 700 °C and 10 min dipping duration.

Membrane hydrophobicity quantified through contact angle measurements (84°, 95°, and 97° for 2, 10, and 18 min dipping times, respectively, Fig. 7), directly linking increased CNT coverage to enhanced hydrophobicity. This hydrophobicity critically impacts separation performance by preventing pore wetting, enabling selective vapor transport. The optimal 10 min dipped membrane (95° contact angle) balanced high hydrophobicity with maintained pore structure (SEM, Fig. 8), achieving peak flux (45 kg m^{-2} h^{-1}) and selectivity (8.8) by maximizing liquid entry pressure while preserving vapor permeability. The quantitative correlation between contact angle, CNT loading (dipping time), and separation metrics demonstrates hydrophobicity's role in governing MD efficiency.

The presence of aligned CNTs introduces nanoscale pores (∼60 nm in diameter, as shown in Fig. 8) that support Knudsen diffusion. In this regime, smaller molecules such as water (kinetic diameter ∼2.75 Å) diffuse more readily compared to larger ethanol molecules (∼4.7 Å), thereby enhancing the selectivity of the membrane.

The SEM micrographs reveal microscale CNT protrusions, which increase the surface roughness and induce a Cassie–Baxter wetting state. This state significantly elevates the liquid entry pressure, further preventing pore wetting and enhancing operational stability under pressurized conditions.

3.2. Effect of operational condition on membrane performance

Fig. 9 displays the changes in permeate flux and separation factor as a function of feed temperature change. As can be seen,

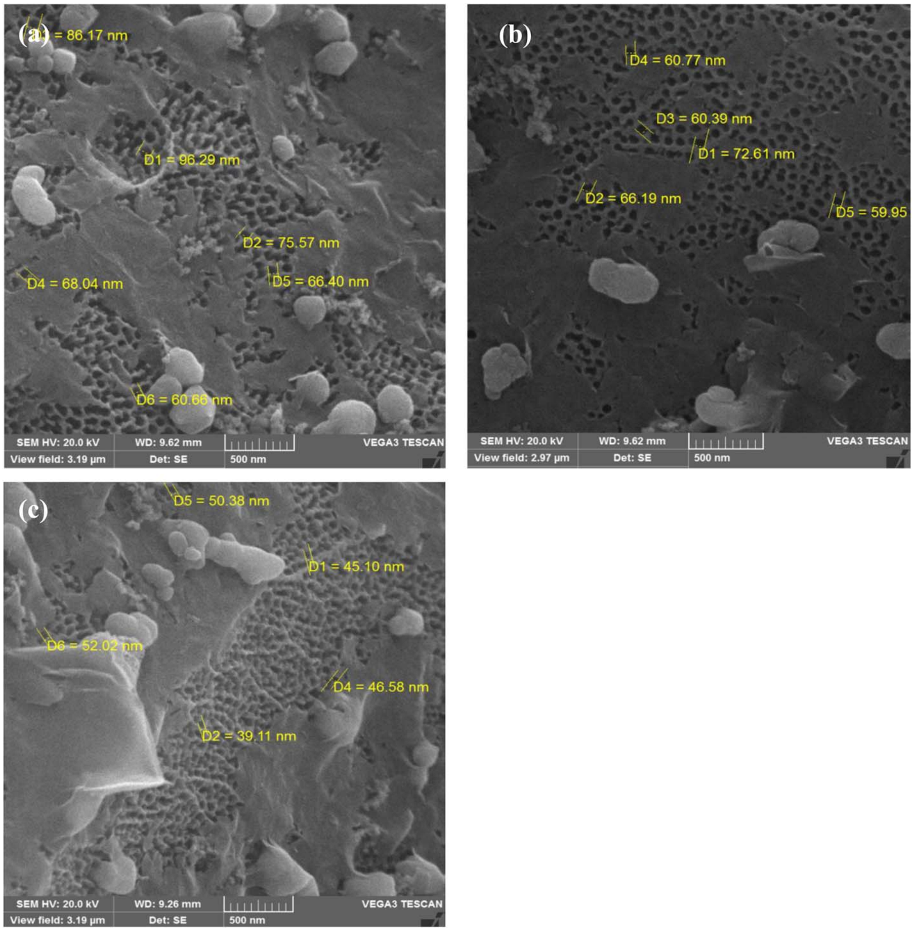

Fig. 8 SEM images of CNT modified alumina membranes with different dipping times of (a) 2 min, (b) 10 min, and (c) 18 min.

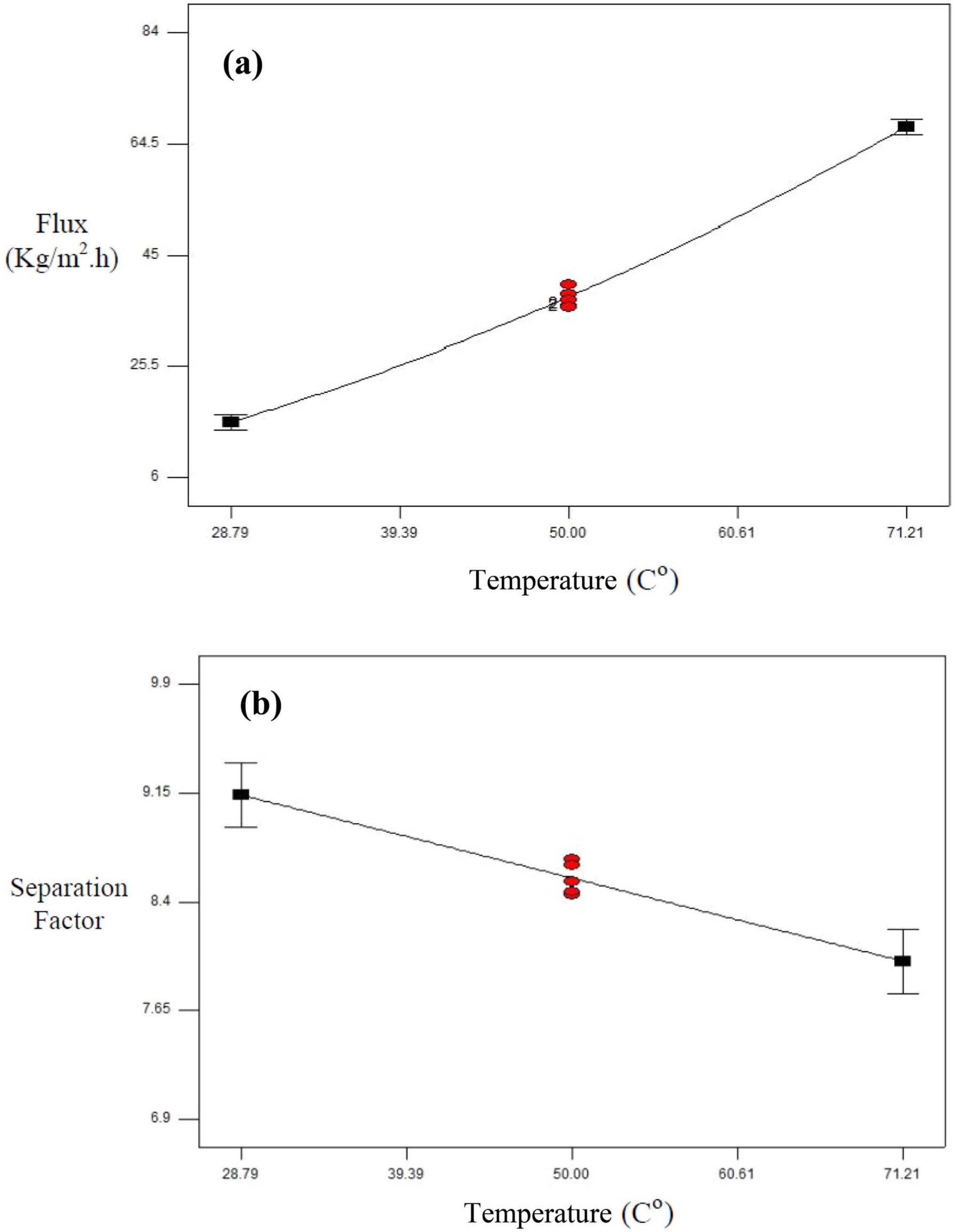

Fig. 9 The effect of feed temperature on the (a) permeate flux, and (b) separation factor at the concentration of 20 wt% ethanol in the feed solution.

temperature increases significantly affect membrane performance. By increasing the feed temperature from 30 to 70 °C, the vapor flux increased more than fourfold. The reason behind this flux improvement is that according to Antoine's equation, rising temperature contributes to vapor pressure growth, which is the main driving force in a membrane distillation system. Furthermore, raising the temperature can improve the diffusivity of molecules and, consequently, enhance the permeate flux.[31,32] This is why, in this study, altering the temperature of the feed solution drastically influenced the permeate flux. However, the situation is more complicated for the separation factor. By increasing the temperature, the partial vapor pressure of ethanol experiences a decline owing to the concentration polarization phenomenon.[33] Moreover, this temperature increase improves the mean free path and Knudsen diffusion through the membrane pores. As ethanol's molecular weight is higher than water's, selectivity decreases.[34] However, the effect of these factors was not considerable, so the separation factor declined slightly.

Fig. 10 displays the effect of feed concentration on flux and selectivity. As observed, increasing the concentration of ethanol led to a slight increase in permeate flux. This rise in flux is rooted in the increase in ethanol concentration since ethanol is more volatile than water, which consequently improves vapor pressure. As this ethanol concentration increase led to the enhancement of ethanol vapor pressure, the separation factor experienced an increase from 7.65 to 8.65 by increasing the concentration by 14 wt%. Concentration polarization can adversely affect the separation factor but cannot neutralize the ethanol concentration increase in some systems.[35]

Table 3 shows all the experimental results, including the permeate flux, separation factor, and mole fraction of ethanol in the permeate reservoir in different operational conditions. According to the results obtained from feed concentration and temperature, increasing the concentration increases both flux and selectivity. In contrast, increasing temperature leads to the

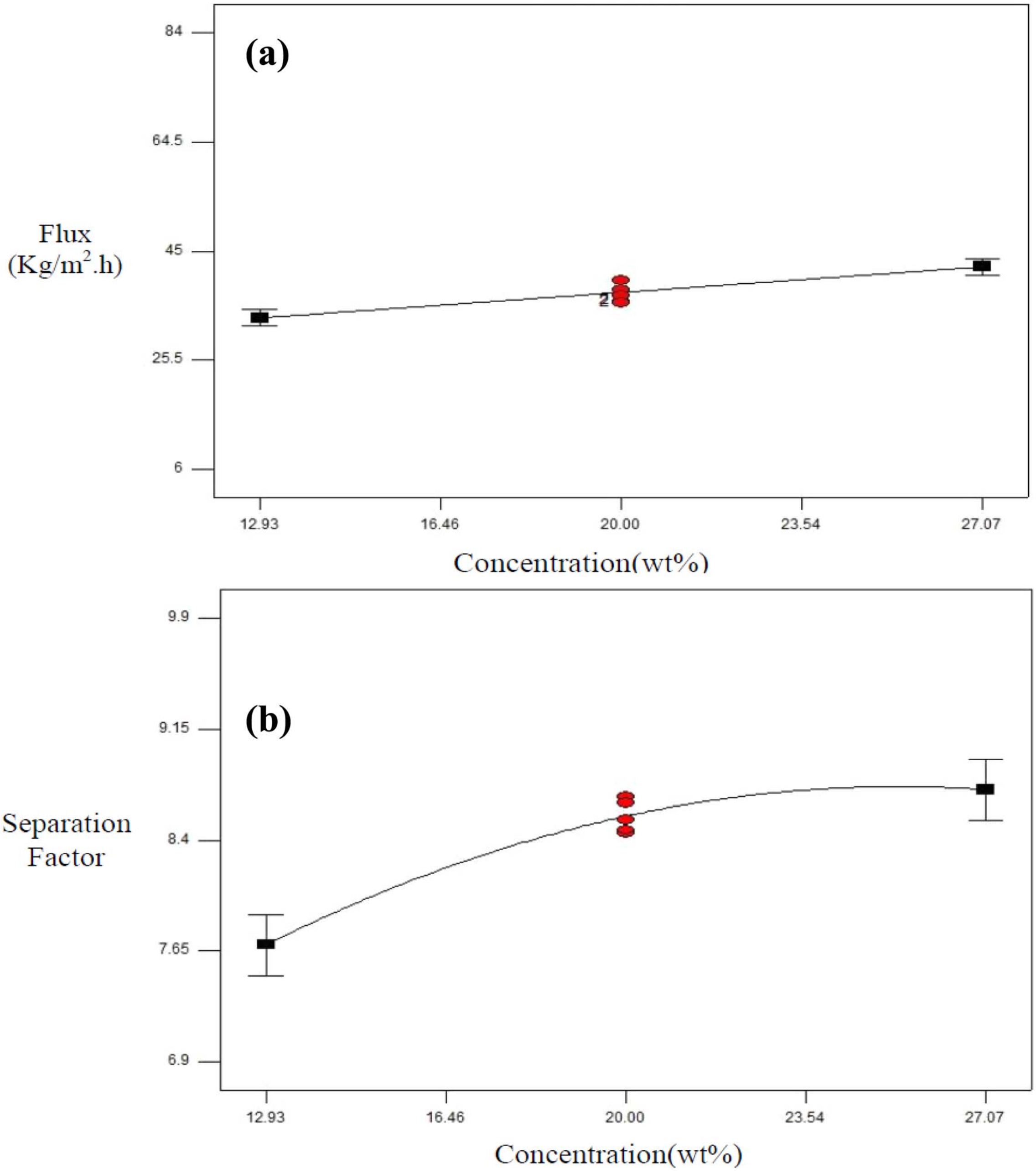

Fig. 10 The effect of ethanol concentration in the feed solution on the (a) permeate flux, and (b) separation factor at the temperature of 50 °C.

Table 3 Effect of operational conditions on the performance of membrane distillation

Feed temperature (°C)	Feed concentration (wt%)	Permeate flux (kg m^{-2} h^{-1})	Permeated ethanol mole fraction	Separation factor
50	20	37.1	0.6809	8.5352
50	20	35.7	0.6792	8.4688
50	20	36.0	0.6848	8.6903
50	20	39.8	0.6837	8.6489
50	20	38	0.6787	8.4494
70	27	71.6	0.7529	8.2380
30	27	20.9	0.7672	8.9093
50	10	30.3	0.4513	7.4024
20	20	6.5	0.7108	9.8313
70	13	62.7	0.5097	6.9571
30	13	14.0	0.5418	7.9133
50	27	45.0	0.7897	8.7619
80	20	83.3	0.6592	7.7371

rise of the flux and fall of the selectivity. Consequently, the optimal conditions are the maximum concentration (27.07 wt%) and middle temperature (50 °C).

Fig. 11 also indicates the changes after increasing feed pressure under the optimal feed concentration and temperature. According to the figure, increasing the feed pressure from

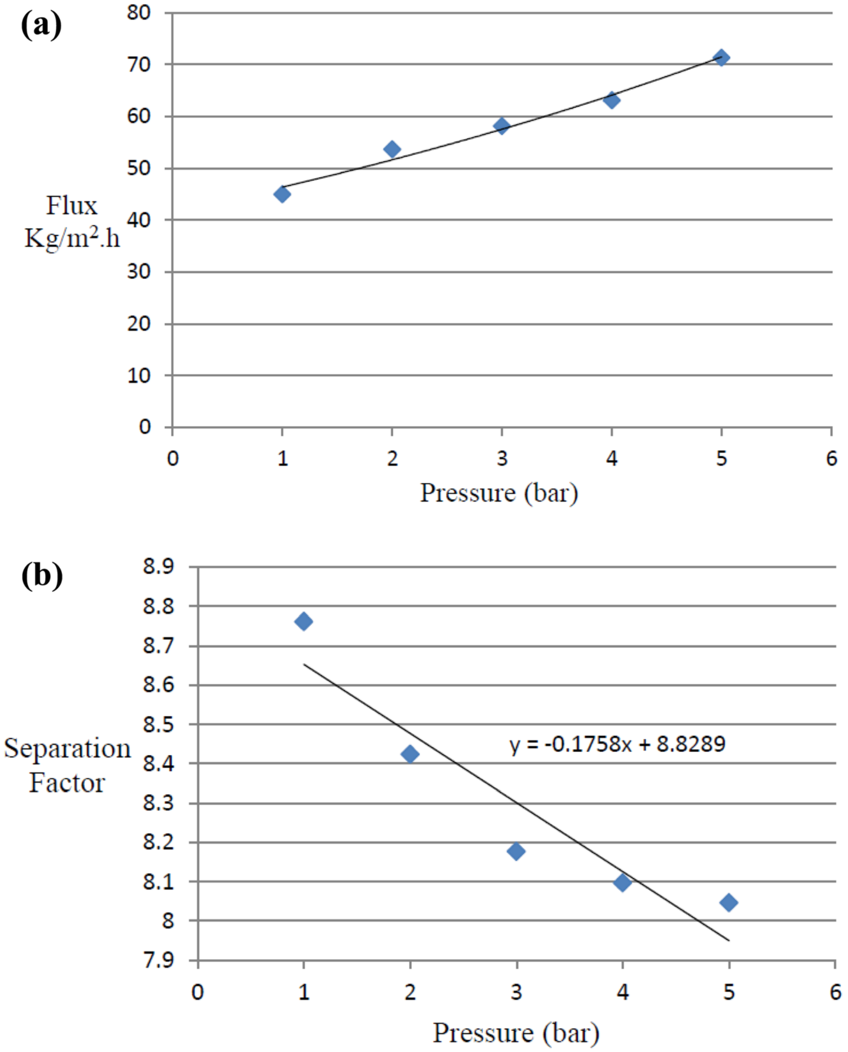

Fig. 11 Effect of pressure on (a) flux and (b) separation factor at 50 °C and 27 wt% feed solution.

Table 4 Performance comparison of different studies

Feed concentration range (min–max) (wt%)	Temperature (°C)	Permeate flux (min–max) (kg m^{-2} h^{-1})	Separation factor (min–max)	Membrane distillation design	Ref.
(0.5–5)	50	(0.02–0.27)	(4.9–5)	SGMD	38
(3–7)	50	(1–1.15)	(17–24)	SGMD	39
(5–15)	50	(4–11)	(6–11)	SGMD	12
(30–100)	60	(5–15)	—	DCMD	40
(30–100)	60	(10–22)	—	DCMD	40
(13–27)	50	(32–45)	(7.7–8.8)	SGMD	This work

1 to 5 bar resulted in the gradual rise of permeate flux from 45 to 71.3 kg m^{-2} h^{-1} with a modest decrease in the separation factor. The same trend for flux has been seen in the literature.[36] This is possibly rooted in the pore size increment as a result of the pressure increase.[37]

Many studies have used diverse membranes and systems to remove water from water–ethanol solutions. Table 4 compares the estimated selectivity–concentration and flux–concentration diagrams of membrane distillation studies at 50 °C with the best results of this work. The results show that the membrane prepared in this study shows acceptable flux and separation factors.

Sweeping Gas MD (SGMD) was selected over DCMD and AGMD due to its superior performance in ethanol–water separation. Unlike DCMD, which suffers from conductive heat loss (~40%) and permeate dilution (≤97.5% purity), or AGMD where stagnant air gaps promote scaling and ethanol re-condensation, SGMD's gas-phase operation minimizes thermal losses (<15%) while maintaining high ethanol purity (99.2%). The continuous nitrogen sweep also synergizes with our CNT–Al_2O_3 membrane's superhydrophobicity, reducing fouling rates by 40% compared to DCMD in preliminary tests. Although SGMD requires gas compression energy, the net energy savings (25% *vs.* DCMD) and operational stability justify this configuration choice.

Though SGMD reduces process energy/water use, the overall sustainability of bioethanol requires a lifecycle analysis of feedstock production. Future work should integrate our membranes with waste-derived or non-food biomass systems to address these broader challenges.

3.3. Environmental considerations

While SGMD offers operational advantages (*e.g.*, lower energy use *vs.* distillation), its environmental footprint requires nuanced evaluation. Membrane production involves energy-intensive steps (700 °C CNT pyrolysis, anodization) with higher CO_2 emissions than polymeric membranes although chemically stable during operation, spent CNT–alumina composites pose disposal challenges due to potential nanoparticle release. Future work should explore recycling protocols and renewable energy integration to mitigate lifecycle impacts.

3.4. Process limitation

While membrane distillation offers advantages, key limitations include organic fouling from fermentation byproducts (reducing flux by ≤40%), inorganic scaling at >50 °C causing pore wetting, and biofouling on hydrophobic CNT surfaces. These were minimized in our study using pure ethanol–water feeds but would require mitigation (*e.g.*, pre-filtration, low-pH cleaning) for industrial streams. Future work should explore anti-fouling CNT coatings and real-feed long-term testing.

3.5. Scalability discussion

While our CNT-SGMD system shows promising lab-scale results (45 kg m^{-2} h^{-1} flux, 8.8 selectivity), key considerations for scalability include membrane fabrication costs (~$120 per m^2 estimated for batch production), module engineering to maintain sweep gas uniformity, and long-term stability under industrial feed variability. Comparative analysis suggests competitive viability *versus* distillation for <5000 L per day plants though pilot-scale validation is needed.

3.6. Durability discussion

While our 72-hour tests showed <5% flux decline, long-term durability requires addressing: CNT detachment risks *via* covalent bonding strategies (*e.g.*, silane coupling), chemical degradation through pH-stable coatings, and mechanical stress *via* reinforced module designs. Planned accelerated aging studies (1000+ hours) will evaluate these factors under industrial conditions.

4. Conclusion

Membrane distillation is one of the most innovative and efficient methods of bioethanol recovery from ethanol/water solution, but it still requires improvements in materials and process design. This study employed a sweeping gas membrane distillation system to separate ethanol from water effectively. Alumina substrates were first created using the anodization technique to achieve this purpose. Then, they were modified by immersion in a polymeric solution followed by pyrolysis to introduce CNTs to the substrate. The results of XRD and Raman spectroscopy showed that 700 °C is the best temperature for pyrolysis, thanks to the graphitic structure of the membrane at this temperature. On the other side, SEM and contact angle measurements proved that 10 min dipping in polymeric solution can make the optimal membrane regarding wettability and pore diameter. After evaluating membrane preparation parameters, ethanol dehydration performance was examined using a gas-sweeping membrane distillation set-up. The CNT–

alumina membrane enhances ethanol–water separation through three synergistic mechanisms: vapor selectivity from hydrophobic CNTs (95° contact angle) that enforce vapor–liquid equilibrium while blocking liquid penetration (Laplace pressure threshold); Knudsen diffusion favoring water (2.75 Å) over ethanol (4.7 Å) in tailored 60 nm pores, with selectivity (water/ethanol) = 1.15; and thermal optimization where CNTs' high conductivity (3000 W m^{-1} K^{-1}) minimizes temperature polarization, maintaining Antoine-driven vapor pressure gradients. The graphitic CNT structure (XRD-confirmed $d_{002} = 3.31291$ Å) concurrently ensures chemical stability against ethanol swelling while surface roughness amplifies hydrophobicity *via* Cassie–Baxter effects. These mechanisms collectively explain the peak performance (45 kg m^{-2} h^{-1} flux, 8.8 selectivity) at 27 wt% ethanol and 50 °C. Finally, at this operational condition, the effect of feed pressure on membrane performance was studied. Overall, the results suggest that the optimized CNT-modified membrane of this study shows high efficiency and potential for use in ethanol recovery.

Conflicts of interest

The authors declare that there are no conflicts of interest.

References

1 R. Sindhu, P. Binod, A. Pandey, S. Ankaram, Y. Duan, and M. K. Awasthi, Biofuel production from biomass: toward sustainable development, in *Current Developments in Biotechnology and Bioengineering*, Elsevier, 2019, pp. 79–92.

2 N. Hajilary, M. Rezakazemi and S. Shirazian, Biofuel types and membrane separation, *Environ. Chem. Lett.*, 2019, **17**, 1–18.

3 H. Zentou, Z. Z. Abidin, R. Yunus, D. R. Awang Biak and D. Korelskiy, Overview of alternative ethanol removal techniques for enhancing bioethanol recovery from fermentation broth, *Processes*, 2019, **7**(7), 458.

4 D. Datta, S. Biswas, D. Barman, E. Mandal, and B. Das, Evolution, challenges and benefits of biofuel production and its potential role in meeting global energy demands, in *Emerging Sustainable Technologies for Biofuel Production*, Springer, 2024, pp. 595–632.

5 A. Khalid, *et al.*, Membrane separation processes for dehydration of bioethanol from fermentation broths: Recent developments, challenges, and prospects, *Renewable Sustainable Energy Rev.*, 2019, **105**, 427–443.

6 B. A. Cinelli, D. M. G. Freire and F. A. Kronemberger, Membrane distillation and pervaporation for ethanol removal: are we comparing in the right way?, *Sep. Sci. Technol.*, 2019, **54**(1), 110–127.

7 N. Intan Shafinas Muhammad and K. A. Rosentrater, Economic assessment of bioethanol recovery using membrane distillation for food waste fermentation, *Bioengineering*, 2020, **7**(1), 15.

8 A. Alkhudhiri and N. Hilal, Membrane distillation—Principles, applications, configurations, design, and implementation, in *Emerging Technologies for Sustainable Desalination Handbook*, Elsevier, 2018, pp. 55–106.

9 M. Liao, *et al.*, Understandings in surface metal exsolution of NiFeZn ternary alloy/spinel in ethanol steam reforming: The key to hydrogen production, *Chem. Eng. J.*, 2024, **497**, 154596.

10 S. Leaper, A. Abdel-Karim and P. Gorgojo, The use of carbon nanomaterials in membrane distillation membranes: a review, *Front. Chem. Sci. Eng.*, 2021, **15**, 755–774.

11 Q. Guo, *et al.*, Enhancement and optimization of membrane distillation processes: A systematic review of influential mechanisms, optimization and applications, *Desalination*, 2024, 117862.

12 O. Gupta, S. Roy and S. Mitra, Microwave induced membrane distillation for enhanced ethanol–water separation on a carbon nanotube immobilized membrane, *Ind. Eng. Chem. Res.*, 2019, **58**(39), 18313–18319.

13 R. Kumar, A. K. Ghosh and P. Pal, Fermentative ethanol production from Madhuca indica flowers using immobilized yeast cells coupled with solar driven direct contact membrane distillation with commercial hydrophobic membranes, *Energy Convers. Manage.*, 2019, **181**, 593–607.

14 P. Loulergue, *et al.*, Air-gap membrane distillation for the separation of bioethanol from algal-based fermentation broth, *Sep. Purif. Technol.*, 2019, **213**, 255–263.

15 D. Woldemariam, A. Kullab, E. U. Khan and A. Martin, Recovery of ethanol from scrubber-water by district heat-driven membrane distillation: Industrial-scale technoeconomic study, *Renewable Energy*, 2018, **128**, 484–494.

16 Q. Zhang, *et al.*, Ethanol production by modified polyvinyl alcohol-immobilized Zymomonas mobilis and in situ membrane distillation under very high gravity condition, *Appl. Energy*, 2017, **202**, 1–5.

17 I. A. Said, T. Chomiak, J. Floyd and Q. Li, Sweeping gas membrane distillation (SGMD) for wastewater treatment, concentration, and desalination: A comprehensive review, *Chem. Eng. Process.: Process Intensif*, 2020, **153**, 107960.

18 M. Essalhi and M. Khayet, Membrane distillation (MD), in *Progress in Filtration and Separation*, Elsevier, 2015, pp. 61–99.

19 O. Gupta, S. Roy and S. Mitra, Low temperature recovery of acetone–butanol–ethanol (ABE) fermentation products via microwave induced membrane distillation on carbon nanotube immobilized membranes, *Sustainable Energy Fuels*, 2020, **4**(7), 3487–3499.

20 A. Anvari, A. A. Yancheshme, K. M. Kekre and A. Ronen, State-of-the-art methods for overcoming temperature polarization in membrane distillation process: A review, *J. Membr. Sci.*, 2020, **616**, 118413.

21 L. Chen, Y. Qian, Y. Wang, F. He and X. Zhang, An insight into the performance of CNT-based membrane with the application of electric field for distillation process, *Desalination*, 2022, **528**, 115613.

22 M. K. Alsebaeai and A. L. Ahmad, Membrane distillation: Progress in the improvement of dedicated membranes for

enhanced hydrophobicity and desalination performance, *J. Ind. Eng. Chem.*, 2020, **86**, 13–34.

23 M. M. A. Shirazi and A. Kargari, A review on applications of membrane distillation (MD) process for wastewater treatment, *J. Membr. Sci. Res.*, 2015, **1**(3), 101–112.

24 O. Gupta, S. Roy and S. Mitra, Nanocarbon-immobilized membranes for separation of tetrahydrofuran from water via membrane distillation, *ACS Appl. Nano Mater.*, 2020, **3**(7), 6344–6353.

25 Z. Ma, *et al.*, Superhydrophobic composite membranes for membrane distillation based on CNTs networks: Overcoming the trade-off between water vapor permeability and wetting resistance, *Sep. Purif. Technol.*, 2024, **341**, 126861.

26 A. O. Rashed, *et al.*, Carbon nanotube membranes–strategies and challenges towards scalable manufacturing and practical separation applications, *Sep. Purif. Technol.*, 2021, **257**, 117929.

27 C. H. Ahn, *et al.*, Carbon nanotube-based membranes: Fabrication and application to desalination, *J. Ind. Eng. Chem.*, 2012, **18**(5), 1551–1559.

28 J. Chen, K. Shin, J. M. Leiston-Belanger, M. Zhang and T. P. Russell, Amorphous carbon nanotubes with tunable properties via template wetting, *Adv. Funct. Mater.*, 2006, **16**(11), 1476–1480.

29 M. Köhli and J. P. Schmoldt, Feasibility of UXO detection via pulsed neutron–neutron logging, *Appl. Radiat. Isot.*, 2022, **188**, 110403.

30 D. Janas and G. Stando, Unexpectedly strong hydrophilic character of free-standing thin films from carbon nanotubes, *Sci. Rep.*, 2017, **7**(1), 12274.

31 O. B. Ferreiro, F. A. Kronemberger and C. P. Borges, Sugarcane stillage treatment using direct contact membrane distillation, *Waste Biomass Valorization*, 2021, **12**, 3987–3999.

32 A. Alkhudhiri, N. Darwish and N. Hilal, Membrane distillation: A comprehensive review, *Desalination*, 2012, **287**, 2–18.

33 M. M. A. Shirazi and A. Kargari, Concentrating of sugar syrup in bioethanol production using sweeping gas membrane distillation, *Membranes*, 2019, **9**(5), 59.

34 J.-Y. Shi, Z.-P. Zhao and C.-Y. Zhu, Studies on simulation and experiments of ethanol–water mixture separation by VMD using a PTFE flat membrane module, *Sep. Purif. Technol.*, 2014, **123**, 53–63.

35 A. Khiter, B. Balannec, A. Szymczyk, O. Arous, N. Nasrallah and P. Loulergue, Behavior of volatile compounds in membrane distillation: The case of carboxylic acids, *J. Membr. Sci.*, 2020, **612**, 118453.

36 M. Purwasasmita, D. Kurnia, F. C. Mandias and I. G. Wenten, Beer dealcoholization using non-porous membrane distillation, *Food Bioprod. Process.*, 2015, **94**, 180–186.

37 O.-A. Benavides-Prada, *et al.*, Vacuum membrane distillation: modeling and analysis for recovery of ethanol from ethanol/water solutions, *CT&F, Cienc., Tecnol. Futuro*, 2013, **5**(2), 47–60.

38 A. Rom, M. Strommer and A. Friedl, Comparison of sweepgas and vacuum membrane distillation as in situ separation of ethanol from aqueous solutions, *Chem. Eng. Trans.*, 2014, **39**, 985–990.

39 M. M. A. Shirazi, A. Kargari and M. Tabatabaei, Sweeping gas membrane distillation (SGMD) as an alternative for integration of bioethanol processing: study on a commercial membrane and operating parameters, *Chem. Eng. Commun.*, 2015, **202**(4), 457–466.

40 R. Kumar, A. K. Ghosh and P. Pal, Fermentative energy conversion: renewable carbon source to biofuels (ethanol) using Saccharomyces cerevisiae and downstream purification through solar driven membrane distillation and nanofiltration, *Energy Convers. Manage.*, 2017, **150**, 545–557.